Article ID: 1000-324X(2022)06-0691-06 **DOI:** 10.15541/jim20210491

Stability of Low-index Surfaces of Cs_2SnI_6 Studied by First-principles Calculations

LIN Aming[1,2], SUN Yiyang[1,2]

(1. Shanghai Institute of Ceramics, Chinese Academy of Sciences, Shanghai 200050, China; 2. University of Chinese Academy of Sciences, Beijing 100049, China)

Abstract: Cs_2SnI_6 is a stable and environmentally friendly halide perovskite material with great potential for photovoltaic and optoelectronic applications. While the surface properties are of paramount importance for device fabrications, there have been no such theoretical studies on this material. Using density functional theory calculations with the SCAN+rVV10 functional, the (001), (011) and (111) surfaces of Cs_2SnI_6 were studied to reveal their thermodynamic stability. We constructed seven models for these surfaces, including two along the (001) orientation (CsI_2- and SnI_4-terminated surfaces), two along the (011) orientation (I_4- and Cs_2SnI_2-terminated surfaces) and three along the (111) orientation (non-stoichiometric CsI_3-, Sn- and stoichiometric CsI_3-terminated surfaces). Because most of the surfaces are non-stoichiometric, their relative stability depends on the experimental preparation condition, which is reflected by the chemical potentials of the constituent elements in the calculation. By determining the allowed chemical potential region, the thermodynamic stability of these Cs_2SnI_6 surfaces is analyzed. The results show that the surface energies of the (001) and (011) surfaces are affected by the chemical potentials, while the stoichiometric CsI_3-terminated (111) surface is unaffected by the chemical potentials and is energetically the most stable surface of Cs_2SnI_6. Thus, the observed exposure of (111) surface of Cs_2SnI_6 crystals in several recent experiments is determined to be driven by thermodynamics.

Key words: perovskite; surface energy; Cs_2SnI_6; photovoltaic material; luminescent material

Organic-inorganic hybrid lead halide perovskites, such as $CH_3NH_3PbI_3$[1–3] have attracted enormous research interests for applications in efficient photovoltaic[4], light-emitting[5] and photodetection devices[6]. As their lead-free counterparts, Sn-based halide perovskites, such as $CH_3NH_3SnI_3$[7–9] and $CsSnI_3$[10–12], have been proposed for such applications because of their nontoxicity. However, because 2+ state is not the most stable valence state of Sn, the Sn-based perovskites are prone to further oxidation, rendering them even less stable than the Pb-based perovskites, which are already well known to have the stability issue[13]. It is highly desirable to develop air-stable alternatives. For this purpose, Cs_2SnI_6 is a promising material, in which Sn is already in 4+ valence state and resistant to further oxidation[14–16]. Meanwhile, it has a suitable band gap and strong optical absorption for photovoltaic applications[17–19].

The halide perovskite materials are usually reported to exhibit defect tolerance in the bulk[20-21]. Therefore, the surfaces, interfaces and grain-boundaries are usually the main concerns for optimizing the device performance. The surface properties of Cs_2SnI_6, which are expected to play an important role in the devices, remain poorly understood. Recently, several groups have devoted to the study on the surfaces of Cs_2SnI_6. Kapil *et al.*[22] suggested the existence of the surface state in Cs_2SnI_6. Shin *et al.*[23] investigated the role of the surface states in the presence of a redox mediator. Xu *et al.*[24] reported a general approach to synthesize layered nanoplatelets of Cs_2SnI_6. Zhu *et al.*[25] revealed that Cs_2SnI_6 crystals have a preferential growth of (111) surface. Several experiments also proved that Cs_2SnI_6 tends to grow along the <111> direction[26–28]. However, it is not clear that this preference is thermodynamically driven or just a result of growth

Received date: 2021-08-05; **Revised date:** 2021-08-20; **Published:** 2021-11-01
Foundation item: Shanghai International Cooperation Project (20520760900)
Biography: LIN Aming (1996–), female, Master candidate. E-mail: linaming@student.sic.ac.cn
林啊鸣(1996–), 女, 硕士研究生. E-mail: linaming@student.sic.ac.cn
Corresponding author: SUN Yiyang, professor. E-mail: yysun@mail.sic.ac.cn
孙宜阳, 研究员. E-mail: yysun@mail.sic.ac.cn

condition specific to individual experiments.

In this work, as motivated by the experimental works, we study the surface properties of Cs_2SnI_6 using first-principles calculations. As an initiative work, we attempt to understand the preference to the (111) surface in different crystal growth experiments. Different surface models with different surface orientations and terminations were set up to compare their thermodynamic stability. As some terminations are non-stoichiometric, to evaluate their relative stability it is necessary to calculate the chemical potentials to consider the crystal growth conditions. By analyzing the surface stability, it is expected to provide useful information for future experimental synthesis and device fabrication.

1 Computational method

Our first-principles calculations were based on density functional theory and performed using the Vienna *Ab initio* Simulation Package (VASP)[29]. Projector augmented wave (PAW) potentials were used to describe the interaction between ion cores and valence electrons[30]. The strongly constrained and appropriately normed (SCAN) functional in combination with the rVV10 van der Waals (vdW) functional was used for the exchange-correlation functional[31]. The cutoff energy of planewave basis set was taken to be 340 eV and the Γ-centered 3×3×3 *k*-point mesh was used for optimizing the 9-atom primitive cell of Cs_2SnI_6. A cutoff energy of 272 eV and a Γ-centered 3×3×1 *k*-point mesh were used for the surface calculations.

2 Results and discussion

Experimentally, it is reported that bulk Cs_2SnI_6 exhibits a cubic structure with Fm-3m space group symmetry, as shown in Fig. 1(a), and the lattice parameter a_0 is 1.165 nm[20]. The calculated a_0 using the SCAN+rVV10 functional is 1.156 nm, 0.8% smaller than the experimental value. The SCAN functional without considering the vdW effect yields a_0=1.178 nm, 1.1% larger than the experimental value, suggesting that the vdW effect is significant for Cs_2SnI_6. For comparison, the commonly used PBE and HSE functional is also considered, which yield a_0=1.203 and 1.197 nm, respectively. The reason for this large vdW effect is that the material is rather soft. The calculated bulk modulus using the SCAN+rVV10 method is only 13.1 GPa. Using the other functionals mentioned above would yield even smaller bulk modulus.

The band structure and projected density of states (pDOS) of Cs_2SnI_6 were calculated, as shown in Fig. 1(b). The direct gap at the Γ point is 0.19 eV, significantly smaller than the experimental band gap of ~1.3 eV, suggesting that the meta-generalized gradient approximation is not sufficient for studying band-gap-sensitive properties of this material, for which the HSE functional including spin-orbit coupling will be necessary[20]. According to the pDOS plot, the top valence bands are mainly contributed by I5p orbitals, while the bottom conduction bands are contributed by both I5p orbitals and Sn5s orbitals. The Sn5s orbitals form a separate band, above which is another band gap and the Sn5p bands.

The surface properties are studied in the next step. We adopt the symmetric slab models for the surfaces, which possess a mirror symmetry through the middle of the slabs. Such models also avoid spurious interaction between periodic slabs due to dipole-dipole interactions. For all calculations, sufficient vacuum region (more than 1-nm-thick) was used to ensure negligible interaction between the slabs. Seven different terminations of Cs_2SnI_6 surface models were considered, as shown in Fig. 2. The non-stoichiometric (001) surfaces were modeled with CsI_2-terminated (or A-termination) and SnI_4-terminated

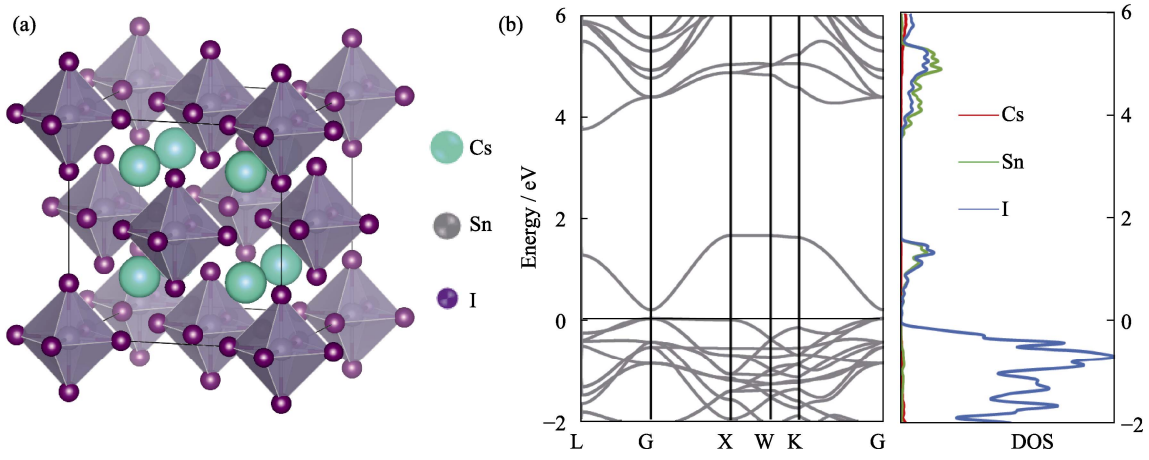

Fig. 1 (a) Atomic structure and (b) band structure and projected density of states (pDOS) of Cs_2SnI_6

Colorful figures are available on website

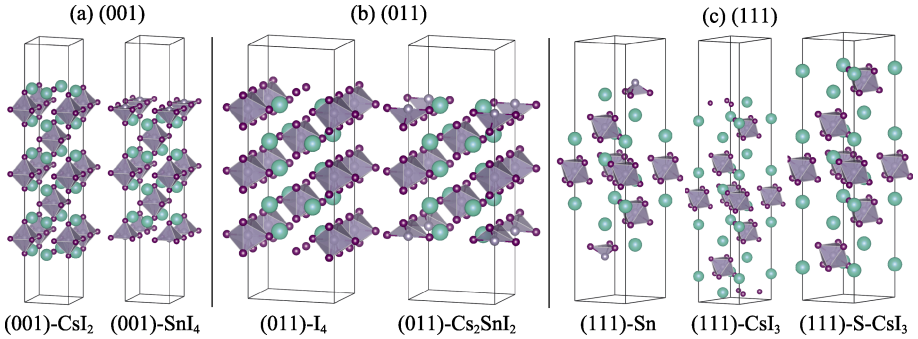

Fig. 2　Seven supercell models of Cs_2SnI_6 surfaces
(a) For (001) surface: CsI_2-terminated and SnI_4-terminated slabs; (b) For (011) surface: I_4-terminated and Cs_2SnI_2-terminated slabs; (c) For (111) surface: non-stoichiometric Sn-terminated, CsI_3-terminated and stoichiometric CsI_3-terminated slabs

(or B-termination) slabs, whose unit-cell formulae were $Cs_{12}Sn_5I_{32}$ and $Cs_8Sn_5I_{28}$, respectively. Similarly, the non-stoichiometric (011) surfaces were modeled with I_4-terminated (A-termination) and Cs_2SnI_2-terminated (B-termination) slabs, whose unit-cell formulae were $Cs_{10}Sn_5I_{34}$ and $Cs_{10}Sn_5I_{26}$, respectively. Along the [111] direction, the atomic stacking sequence is –Sn–CsI_3– CsI_3–Sn–. Correspondingly, the non-stoichiometric Sn-terminated (A-termination), non- stoichiometric CsI_3-terminated (B-termination) and stoichiometric CsI_3-terminated surfaces were modeled, whose unit-cell formulae were $Cs_8Sn_5I_{24}$, $Cs_{12}Sn_5I_{26}$ and $Cs_{10}Sn_5I_{30}$, respectively.

The cleavage energy are firstly evaluated, which is the energy required to split a crystal into two complementary non-stoichiometric terminations. It is noted that CsI_2- and SnI_4-terminations for Cs_2SnI_6 (001) surfaces are mutually complementary, and so are I_4- and Cs_2SnI_2-terminated slabs for (011) surfaces, as well as Sn- and CsI_3-terminated slabs for (111) surfaces. As two complementary surfaces (also referred to as A- and B-termination above) are created simultaneously when a crystal is cleaved, the total cleavage energy of two complementary surfaces can be obtained by

$$E_{\mathrm{cl}}(\mathrm{A}+\mathrm{B})=\frac{1}{2S}\left[E(\mathrm{A})_{\mathrm{slab}}^{\mathrm{unrel}}+E(\mathrm{B})_{\mathrm{slab}}^{\mathrm{unrel}}-nE_{\mathrm{bulk}}\right] \quad (1)$$

where $E(\mathrm{A})_{\mathrm{slab}}^{\mathrm{unrel}}$ and $E(\mathrm{B})_{\mathrm{slab}}^{\mathrm{unrel}}$ are the energies of unrelaxed A- and B-terminated slabs, respectively. E_{bulk} is the energy per unit cell, S represents the surface area and n is the total number of bulk unit cells in the two slabs. Next, the relaxation energy of A-terminated surfaces with both sides relaxed is calculated according to

$$E_{\mathrm{rel}}(\mathrm{A})=\frac{1}{2S}\left[E(\mathrm{A})_{\mathrm{slab}}^{\mathrm{rel}}-E(\mathrm{A})_{\mathrm{slab}}^{\mathrm{unrel}}\right] \quad (2)$$

where $E(\mathrm{A})_{\mathrm{slab}}^{\mathrm{rel}}$ is the energy of A-terminated slab after relaxation. $E_{\mathrm{rel}}(\mathrm{B})$ is calculated similarly. Finally, the total surface energy of the two complementary surfaces can be obtained as the sum of the cleavage and relaxation energies:

$$E_{\mathrm{surf}}(\mathrm{A}+\mathrm{B})=E_{\mathrm{cl}}(\mathrm{A}+\mathrm{B})+E_{\mathrm{rel}}(\mathrm{A})+E_{\mathrm{rel}}(\mathrm{B}) \quad (3)$$

The calculated results of total cleavage energy, total relaxation energy and total surface energy of the two complementary non-stoichiometric terminations with different surface orientations are shown in Fig. 3. For comparison, the cleavage, relaxation and surface energies of the stoichiometric CsI_3-terminated (111) surface are also shown. It can be seen that the total surface energies of the two complementary non-stoichiometric terminations are relatively high compared with that of stoichiometric CsI_3-terminated (111) surface whose surface energy is only 0.11 J/m^2, regardless of the surface orientations. However, the contributions to the cleavage energy from the A- and B-terminations are not equal. Further study is needed to determine whether A- or B-termination could individually have surface energy lower than 0.11 J/m^2. In order to evaluate the relative stability of each surface termination under various experimentally preparation conditions, the consideration of chemical potential μ_{Cs}, μ_{Sn} and μ_{I} is necessary[21,32].

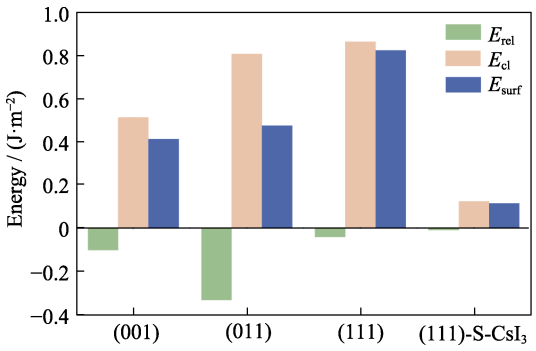

Fig. 3　Calculated total cleavage, relaxation and surface energies of two complementary non-stoichiometric terminations in (001), (011) and (111) orientations, which are compared with the cleavage, relaxation and surface energies of the stoichiometric CsI_3-terminated (111) surface

Through varying the chemical potentials, different experimental conditions can be simulated. The relative values of the chemical potentials of Cs, Sn and I are introduced with respect to their most stable phases, $\Delta\mu_{Cs}=\mu_{Cs}-E_{Cs}^{bulk}$, $\Delta\mu_{Sn}=\mu_{Sn}-E_{Sn}^{bulk}$ and $\Delta\mu_{I}=\mu_{I}-\frac{1}{2}E_{I_2}^{bulk}$. The chemical potentials of Cs, Sn and I are constrained by the calculated enthalpy of formation of the primary phase Cs_2SnI_6[33-34]

$$2\Delta\mu_{Cs}+\Delta\mu_{Sn}+6\Delta\mu_{I}=\Delta E_f\left(Cs_2SnI_6\right) \quad (4)$$

where $\Delta E_f\left(Cs_2SnI_6\right)$ is calculated to be −9.16 eV. The chemical potentials are further subject to specific bounds that are set by the existence of secondary phases:

$$\Delta\mu_{Cs}+\Delta\mu_{Sn}+3\Delta\mu_{I}\leqslant\Delta E_f\left(CsSnI_3\right)=-5.0\ \text{eV} \quad (5)$$

$$\Delta\mu_{Sn}+4\Delta\mu_{I}\leqslant\Delta E_f\left(SnI_4\right)=-1.70\ \text{eV} \quad (6)$$

$$\Delta\mu_{Sn}+2\Delta\mu_{I}\leqslant\Delta E_f\left(SnI_2\right)=-1.37\ \text{eV} \quad (7)$$

$$\Delta\mu_{Cs}+3\Delta\mu_{I}\leqslant\Delta E_f\left(CsI_3\right)=-3.76\ \text{eV} \quad (8)$$

$$\Delta\mu_{Cs}+\Delta\mu_{I}\leqslant\Delta E_f\left(CsI\right)=-3.51\ \text{eV} \quad (9)$$

The enthalpies of formation above were all obtained by SCAN+rVV10 calculations. By considering these constraints, the final allowed region for μ_{Sn} and μ_{I} is demarcated by the points A, B, C, D and E, where equilibrium growth of bulk Cs_2SnI_6 is possible, as shown in Fig. 4.

Using the determined chemical potential region, the surface energy for each individual termination can be obtained using[35-36]

$$E_{surf}\left(A\right)=\frac{1}{2S}\left[E_{slab}\left(A\right)-N_{Cs}\mu_{Cs}-N_{Sn}\mu_{Sn}-N_{I}\mu_{I}\right] \quad (10)$$

where E_{slab} is the total energy of relaxed A-termination, N_{Cs}, N_{Sn} and N_{I} are the numbers of Cs, Sn and I atoms in the slab, respectively. Considering the variation of chemical potential with reference phase as mentioned above, the surface energy can be finally rewritten as

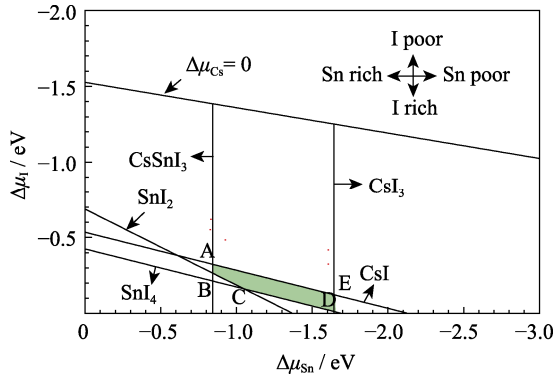

Fig. 4 Illustration of the accessible chemical potential region for Cs_2SnI_6

Constraints imposed by the formation of competing secondary phases resulting in the allowed region shaded in green

$$E_{surf}\left(A\right)=\varnothing\left(A\right)+\frac{1}{2S}\left[\left(\frac{N_{Cs}}{2}-N_{Sn}\right)\Delta\mu_{Sn}+\left(3N_{Cs}-N_{I}\right)\Delta\mu_{I}\right] \quad (11)$$

$$\text{with}\quad \varnothing\left(A\right)=\frac{1}{2S}\left[E_{slab}\left(A\right)-\frac{N_{Cs}}{2}E_{bulk}+\left(\frac{N_{Cs}}{2}-N_{Sn}\right)E_{Sn}^{bulk}+\frac{1}{2}\left(3N_{Cs}-N_{I}\right)E_{I_2}^{bulk}\right] \quad (12)$$

Here, $\varnothing\left(A\right)$ is a constant term, independent of the chemical potentials. Considering that surfaces will spontaneously form and the crystal will be destroyed if surface energy is negative, it is necessary to satisfy $E_{surf}\left(A\right)>0$.

The stability diagram of the Cs_2SnI_6 (001) surface is shown in Fig. 5(a). The blue and orange regions represent the regions where CsI_2- and SnI_4-terminations are stable, respectively. The upper part of the green region is located in the blue region, indicating that the CsI_2-termination is favored under the I-poor condition. There is still a small part of the green region located in the orange region, *e.g.*, at chemical potential points C and D, indicating that the SnI_4-termination is more stable than the CsI_2-termination under I-rich condition.

Similarly, the stability diagram of the Cs_2SnI_6 (011) surface is shown in Fig. 5(b). The blue region represents that the Cs_2SnI_2-termination is thermodynamically more stable, while the orange part refers to the region where the I_4-termination is more stable. It can be seen that the green region is also located in both blue and orange regions, indicating that different terminations are favored when varying the experimental environments. Under I-rich condition (*e.g.*, at chemical potential point A) the Cs_2SnI_2-termination is favored, while under I-poor condition (*e.g.*, the chemical point D) the I_4-termination is favored.

In Fig. 5(c), the stability diagram of Cs_2SnI_6 (111) surface is shown. Different from the stability diagrams of the (001) and (011) surfaces discussed above, the whole green region is located in the orange region for the (111) surface, indicating that the stoichiometric CsI_3-terminated (111) surface is the most energetically favored among the three terminations regardless of the chemical potentials.

Finally, the surface energies of the seven terminations of Cs_2SnI_6 low-index surfaces are compared in Fig. 5(d) as a function of the chemical potentials. It can be seen that the stoichiometric CsI_3-terminated (111) surface consistently has the lowest surface energy, indicating that it is the most thermodynamically favored surface among the seven terminations, in agreement with the recent experimental reports[25-26].

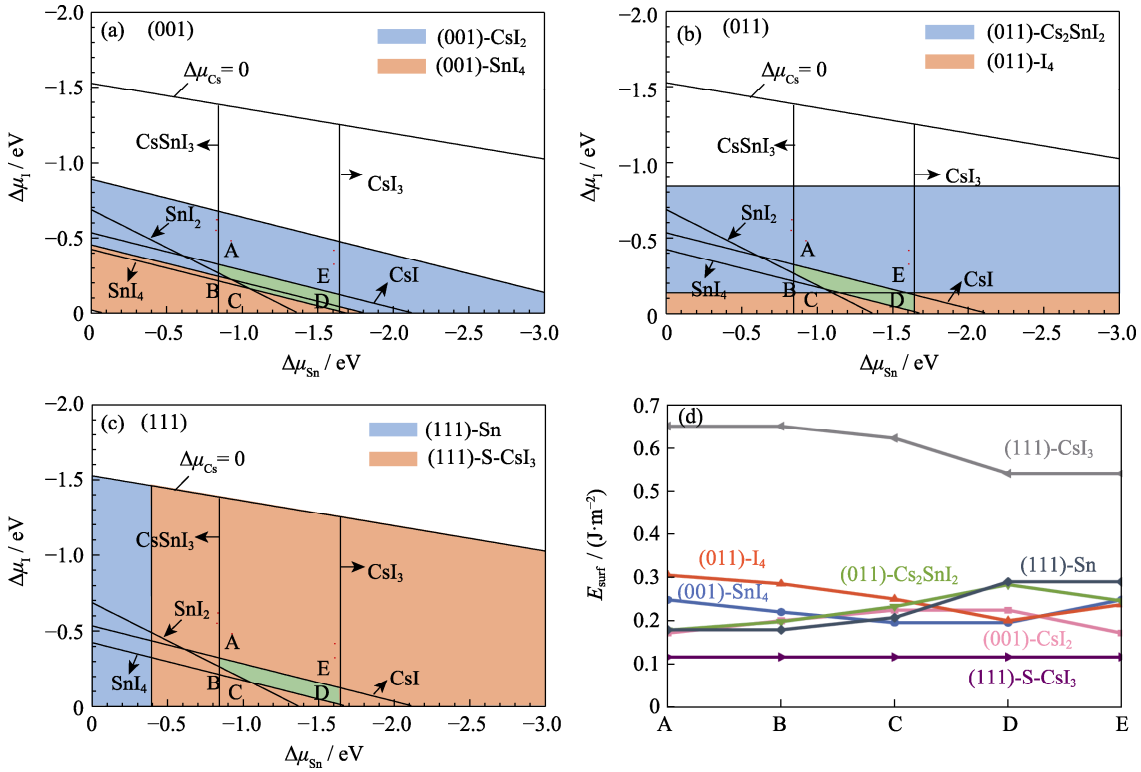

Fig. 5　Stability of low-index surfaces of Cs_2SnI_6 as a function of chemical potentials

(a) Analysis of stability of the two terminations of Cs_2SnI_6 (001) surface with respect to the allowed region for maintaining equilibrium with the primary phase Cs_2SnI_6. The orange and blue regions indicate the stable region for CsI_2- and SnI_4-terminations, respectively; (b) Similar to (a) for the Cs_2SnI_6 (011) surface. The orange and blue regions are for the I_4- and Cs_2SnI_2-terminations, respectively; (c) Similar to (a) for the Cs_2SnI_6 (111) surface. The orange and blue regions are for the Sn- and stoichiometric CsI_3-terminations, respectively; (d) Surface energies of the seven surface models of Cs_2SnI_6 as a function of the chemical potentials. Colorful figures are available on website

3　Conclusion

Based on density-functional theory calculations with the SCAN+rVV10 functional, seven models for the low-index Cs_2SnI_6 surfaces were studied with different surface orientations and terminations to compare their thermodynamic stability. Overall, based on the calculated surface energies, we identified that the stoichiometric CsI_3-termination for (111) surface is consistently the most stable, regardless of the chemical potentials, which is in agreement with the experimental observation that the (111) surface is often the most exposed surface. For the (100) and (110) surfaces, two different terminations were considered for each of them. Their relative stability depends on the chemical potentials. From an experimental point of view, when preparing these two surfaces, different terminations can be obtained by varying the growth condition, *e.g.*, by controlling the I-poor or I-rich conditions.

Acknowledgement

The authors thank Professor Lian Jie, Dr. Zhu Weiguang and Shen Junhua from Rensselaer Polytechnic Institute for enlightening discussions.

References:

[1] STRANKS S D, EPERON G E, GRANCINI G, *et al*. Electron-hole diffusion lengths exceeding trihalide perovskite absorber. *Science*, 2013, **342(6156):** 341–344.

[2] HEO J H, IM S H, NOH J H, *et al*. Efficient inorganic-organic hybrid heterojunction solar cells containing perovskite compound and polymeric hole conductors. *Nature Photonics*, 2013, **7:** 486–491.

[3] SHAO Y, XIAO Z, BI C, *et al*. Origin and elimination of photocurrent hysteresis by fullerene passivation in $CH_3NH_3PbI_3$ planar heterojunction solar cells. *Nature Communications*, 2014, **5:** 5784.

[4] XING G, MATHEWS N, LIM S S, *et al*. Long-range balanced electron- and hole-transport lengths in organic-inorganic $CH_3NH_3PbI_3$. *Science*, 2013, **342(6156):** 344–347.

[5] TAN Z K, MOGHADDAM R S, LAI M L, *et al*. Bright light-emitting diodes based on organometal halide perovskite. *Nature Nanotechnology*, 2014, **9:** 687–692.

[6] GAO L, ZENG K, GUO J, *et al*. Passivated single-crystalline $CH_3NH_3PbI_3$ nanowire photodetector with high detectivity and polarization sensitivity. *Nano Letters*, 2016, **16(12):** 7446–7454.

[7] HAO F, STOUMPOS C C, CAO D H, *et al*. Lead-free solid-state organic-inorganic halide perovskite solar cells. *Nature Photonics*, 2014, **8:** 489–494.

[8] STOUMPOS C C, MALLIAKAS C D, KANATZIDIS M G. Semiconducting tin and lead iodide perovskites with organic cations: phase transitions, high mobilities, and near-infrared photoluminescent properties. *Inorganic Chemistry*, 2013, **52(15):** 9019–9038.

[9] NOEL N K, STRANKS S D, ABATE A, *et al*. Lead-free organic-inorganic tin halide perovskites for photovoltaic applications. *Energy and Environmental Science*, 2014, **7(9):** 3061–3068.

[10] CHUNG I, LEE B, HE J, *et al*. All-solid-state dye-sensitized solar

cells with high efficiency. *Nature*, 2012, **485:** 486–489.
[11] KUMAR M H, DHARANI S, LEONG W L, *et al*. Lead-free halide perovskite solar cells with high photocurrents realized through vacancy modulation. *Advanced Materials*, 2014, **26(41):** 7122–7127.
[12] MARSHALL K P, WALKER M, WALTON R I, *et al.* Enhanced stability and efficiency in hole-transport-layer-free $CsSnI_3$ perovskite photovoltaics. *Nature Energy*, 2016, **1:** 16178.
[13] CHUNG I, SONG J H, IM J, *et al.* $CsSnI_3$: semiconductor or metal? high electrical conductivity and strong near-infrared photoluminescence from a single material. high hole mobility and phase-transitions. *Journal of the American Chemical Society*, 2012, **134(20):** 8579–8587.
[14] LEE B, STOUMPOS C C, ZHOU N, *et al.* Air-stable molecular semiconducting iodosalts for solar cell applications: Cs_2SnI_6 as a hole conductor. *Journal of the American Chemical Society*, 2014, **136(43):** 15379–15385.
[15] SAPAROV B, SUN J P, MENG W, *et al*. Thin-film deposition and characterization of a Sn-deficient perovskite derivative Cs_2SnI_6. *Chemistry of Materials*, 2016, **28(7):** 2315–2322.
[16] QIU X, CAO B, YUAN S, *et al*. From unstable $CsSnI_3$ to air-stable Cs_2SnI_6: a lead-free perovskite solar cell light absorber with bandgap of 1.48 eV and high absorption coefficient. *Solar Energy Materials and Solar Cells*, 2017, **159:** 227–234.
[17] WANG X D, HUANG Y H, LIAO J F, *et al. In situ* construction of a Cs_2SnI_6 perovskite nanocrystal/SnS_2 nanosheet heterojunction with boosted interfacial charge transfer. *Journal of the American Chemical Society*, 2019, **141(34):** 13434–13441.
[18] LIU F, DING C, ZHANG Y, *et al.* Colloidal synthesis of air-stable alloyed $CsSn_{1-x}PbxI_3$ perovskite nanocrystals for use in solar cells. *Journal of the American Chemical Society*, 2017, **139(46):** 16708–16719.
[19] DOLZHNIKOV D S, WANG C, XU Y, *et al.* Ligand-free, quantum-confined Cs_2SnI_6 perovskite nanocrystals. *Chemistry of Materials*, 2017, **29(18):** 7901–7907.
[20] MAUGHAN A E, GANOSE A M, BORDELON M M, *et al*. Defect tolerance to intolerance in the vacancy-ordered double perovskite semiconductors Cs_2SnI_6 and Cs_2TeI_6. *Journal of the American Chemical Society*, 2016, **138(27):** 8453–8464.
[21] XIAO Z, ZHOU Y, HOSONO H, *et al.* Intrinsic defects in a photovoltaic perovskite variant Cs_2SnI_6. *Physical Chemistry Chemical Physics*, 2015, **17(29):** 18900–18903.
[22] KAPIL G, OHTA T, KOYANAGI T, *et al*. Investigation of interfacial charge transfer in solution processed Cs_2SnI_6 thin films. *Journal of Physical Chemistry C*, 2017, **121(24):** 13092–13100.
[23] SHIN H O, KIM B M, JANG T, *et al.* Surface state-mediated charge transfer of Cs_2SnI_6 and its application in dye-sensitized solar cells. *Advanced Energy Materials*, 2019, **9(3):** 1803243.
[24] XU Y, LI S, ZHANG Z, *et al.* Ligand-mediated synthesis of colloidal Cs_2SnI_6 three-dimensional nanocrystals and two-dimensional nanoplatelets. *Nanotechnology*, 2019, **30(29):** 295601.
[25] ZHU W, SHEN J, LI M, *et al*. Kinetically controlled growth of sub-millimeter 2D Cs_2SnI_6 nanosheets at the liquid–liquid interface. *Small*, 2021, **17(4):** 2006279.
[26] LUO R, ZHANG S, ZHAO S, *et al*. Ultrasmall blueshift of near-infrared fluorescence in phase-stable Cs_2SnI_6 thin films. *Physical Review Applied*, 2020, **14(1):** 014048.
[27] ZHOU P, CHEN H, CHAO Y, *et al.* Single-atom Pt-I_3 sites on all-inorganic Cs_2SnI_6 perovskite for efficient photocatalytic hydrogen production. *Nature Communications*, 2021, **12:** 4412.
[28] ULLAH S, ULLAH S, WANG J, *et al*. Investigation of air-stable Cs_2SnI_6 films prepared by the modified two-step process for lead-free perovskite solar cells. *Semiconductor Science and Technology*, 2020, **35:** 125027.
[29] KRESSE G, FURTHMÜLLER J. Efficient iterative schemes for *ab initio* total-energy calculations using a plane-wave basis set. *Physical Review B*, 1996, **54(16):** 11169–11186.
[30] KRESSE G, JOUBERT D. From ultrasoft pseudopotentials to the projector augmented-wave method. *Physical Review B*, 1999, **59(3):** 1758–1775.
[31] PENG H, YANG Z H, PERDEW J P, *et al.* Versatile van der Waals density functional based on a meta-generalized gradient approximation. *Physical Review X*, 2016, **6(4):** 041005.
[32] XIAO Z, LEI H, ZHANG X, *et al.* Ligand-hole in [SnI_6] unit and origin of band gap in photovoltaic perovskite variant Cs_2SnI_6. *Bulletin of the Chemical Society of Japan*, 2015, **88(9):** 1250–1255.
[33] ZHANG S B, NORTHRUP J E. Chemical potential dependence of defect formation energies in GaAs: application to Ga self-diffusion. *Physical Review Letters*, 1991, **67(17):** 2339–2342.
[34] VAN DE WALLE C G, NEUGEBAUER J. First-principles calculations for defects and impurities: applications to III-nitrides. *Journal of Applied Physics*, 2004, **95(8):** 3851–3879.
[35] CHEN H, DING Y H, YU H T, *et al.* First-principles investigation of the electronic properties and stabilities of the $LaAlO_3$ (001) and (110) (1 × 1) polar terminations. *Journal of Physical Chemistry C*, 2015, **119(17):** 9364–9374.
[36] HUANG X, PAUDEL T R, DOWBEN P A, *et al*. Electronic structure and stability of the $CH_3NH_3PbBr_3$ (001) surface. *Physical Review B*, 2016, **94(19):** 195309.

Cs_2SnI_6低指数晶面稳定性的第一性原理计算研究

林啊鸣[1,2], 孙宜阳[1,2]

(1. 中国科学院 上海硅酸盐研究所, 上海 201899; 2. 中国科学院大学, 北京 100049)

摘 要: Cs_2SnI_6是一种稳定且环保的卤化物钙钛矿材料, 在光伏和光电应用方面具有巨大潜力。虽然表面性质对于光电器件的制备至关重要, 但目前尚没有对该材料开展相关的理论研究。利用密度泛函理论计算结合 SCAN+rVV10 泛函, 本工作研究了 Cs_2SnI_6的(001)、(011)和(111)表面以揭示其热力学稳定性。针对每个表面, 研究考虑了具有不同截断的模型, 包括两个沿(001)方向(分别为 CsI_2 和 SnI_4 终止的表面), 两个沿(011)方向(分别为 I_4 和 Cs_2SnI_2 终止的表面)和三个沿(111)方向(分别为非化学计量比的 CsI_3、Sn 和满足化学计量比的 CsI_3 终止的表面)。由于大多数表面模型是非化学计量比的, 它们的相对稳定性取决于实验制备条件, 因此需要考虑组成元素的化学势。通过确定允许的化学势区域, 研究分析了这些表面的热力学稳定性。结果表明, (001)和 (011)面的表面能会受到化学势的影响, 而满足化学计量比的 CsI_3 终止的(111)表面不受化学势影响, 是 Cs_2SnI_6 最稳定的表面。该结果说明, 近期实验普遍观察到的暴露(111)面的晶体是受热力学稳定性驱动形成的。

关 键 词: 钙钛矿; 表面能; Cs_2SnI_6; 光伏材料; 发光材料

中图分类号: TQ174 **文献标志码:** A